Nanoscale

Combined plasmonic Au-nanoparticle and conducting metal oxide high-temperature optical sensing with LSTO

Journal:	*Nanoscale*
Manuscript ID	NR-ART-04-2020-003306.R1
Article Type:	Paper
Date Submitted by the Author:	16-Jun-2020
Complete List of Authors:	Wuenschell, Jeffrey; National Energy Technology Laboratory, U.S. Department of Energy Jee, Youngseok; National Energy Technology Laboratory, Lau, Derek; National Energy Technology Laboratory, U.S. Department of Energy Yu , Yang; U.S. DOE, National Energy Technology Laboratory , ; AECOM, Ohodnicki, Paul; National Energy Technology Laboratory,

ARTICLE

Combined plasmonic Au-nanoparticle and conducting metal oxide high-temperature optical sensing with LSTO

Received 00th January 20xx,
Accepted 00th January 20xx

DOI: 10.1039/x0xx00000x

Jeffrey K. Wuenschell,*[a,b] Youngseok Jee [a,b], Derek K. Lau [a,c], Yang Yu[a],and Paul R. Ohodnicki, Jr.[a†]

Fiber optic sensor technology offers several advantages for harsh-environment applications. However, the development of optical gas sensing layers that are stable under harsh environmental conditions is an ongoing research challenge. In this work, electronically conducting metal oxide lanthanum-doped strontium titanate (LSTO) films embedded with gold nanoparticles are examined as a sensing layer for application in reducing gas flows at high temperature (600-800°C). A strong localized surface plasmon resonance (LSPR) based response to hydrogen is demonstrated in the visible region of the spectrum, while a Drude free electron-based response is observed in the near-IR. Characteristics of these responses are studied both on planar glass substrates and on silica fibers. Charge transfer between the oxide film and the gold nanoparticles is explored as a possible mechanism governing the Au LSPR response and is considered in terms of the corresponding properties of the conducting metal oxide-based matrix phase. Principal component analysis is applied to the combined plasmonic and free-carrier based response over a range of temperatures and hydrogen concentrations. It is demonstrated that the combined visible and near-IR response of these films provides improved versatility for multiwavelength interrogation, as well as improved discrimination of important process parameters (concentration and temperature) through application of multivariate analysis techniques.

Introduction

Processes involving high-temperature or strongly chemically reactive conditions are inherent in many economically and scientifically important applications. Examples include power plants[1-3], emerging power generation technologies such as solid oxide fuel cell (SOFC) monitoring[4], manufacturing processes, and aerospace applications to name a few[5-7]. However, conditions associated with these systems and applications limit the *in-situ* use of many traditional sensor technologies. Although the development of harsh environment sensors presents many materials science challenges, the rapid development of new data analysis tools in artificial intelligence and machine learning drives the need for the collection of quality sensor data. New analytical tools in conjunction with previously inaccessible *in-situ* data promises great rewards from the standpoint of process improvement and optimization. The ability to simultaneously interrogate optical response at multiple wavelengths presents a major advantage over chemi-resistive sensors and creates opportunity for potential realization of a "photonic nose" device – an optical analogue of the electronic nose array approach requiring only a single optical sensor element. Importantly, this device is compatible with harsh environment applications, for which electronic nose array-based sensors are not suited, through eliminating the large numbers of wires and electronic contacts which serve as high probability sources of failure in high temperature and harsh environment sensing applications. Application of multivariate techniques can dramatically simplify complex optical spectra and pull out the most meaningful components of the response (dimensionality reduction). The same techniques can also be used to more optimally select light source and detector combinations for better sensor response, discrimination, and/or cost-efficiency.

Optical fiber-based sensing is well-suited to harsh environment sensing – standard, commercially available silica fiber has been demonstrated suitable for high temperature sensing applications spanning from ~300-1000°C depending upon the ambient atmosphere and protective packaging. Emerging single crystal fibers, such as sapphire for example, offer stability in even more extreme conditions if suitable cladding layers can be identified and developed[8].

Optical-fiber based gas sensing typically relies on a functional thin film layer that responds optically to differing gas environments, either via changes in absorption or refractive index. For harsh environment applications, metal oxide films are commonly utilized for their combination of high temperature stability and free-carrier driven optical response in the NIR with conducting metal oxides showing particularly strong responses[9-14]. Strontium titanate ($SrTiO_3$ - STO) is a high temperature stable oxide that exhibits a perovskite crystal structure. Perovskites are characterized by the ability to accept

[a.] *National Energy Technology Laboratory, 626 Cochrans Mill Rd., P.O. Box 10940, Pittsburgh, PA 15236-0940, USA.*
[b.] *Leidos Research Support Team, 626 Cochrans Mill Rd., P.O. Box 10940, Pittsburgh, PA 15236-0940, USA.*
[c.] *ORISE, 626 Cochrans Mill Rd., P.O. Box 10940, Pittsburgh, PA 15236-0940, USA.*
† Currently at the University of Pittsburgh, Pittsburgh, PA.
Electronic Supplementary Information (ESI) available: [details of any supplementary information available should be included here]. See DOI: 10.1039/x0xx00000x

large concentrations of dopant atoms without destabilizing the crystal structure. For this reason, doped STO and related compounds – e.g., strontium manganite, strontium ferrite, barium titanate, lanthanum titanate, lanthanum aluminate etc. – are heavily studied and are known to exhibit a wide range of valuable electrical, magnetic, optical, and chemical characteristics[15, 16]. In the strontium titanate system, La is used as an n-type dopant, replacing strontium atoms at the A-site positions of the perovskite unit cell (substituting Sr^{2+} ions with La^{3+} ions) and significantly increasing the electrical conductivity to enhance the near-IR optical sensing response. Lanthanum-doped strontium titanate ($La_xSr_{1-x}TiO_3$) has been shown to maintain the perovskite phase at dopant concentrations as high as x = 0.4, enabling high corresponding carrier concentrations at high-temperature and in reducing conditions[17,18]. The population of cation and oxygen vacancies within LSTO at high-temperature is believed to be strongly dependent upon the oxygen partial pressure (pO_2), which in turn impacts the free-carrier density. The mechanisms suggested in the literature[17, 19, 20] can be summarized as follows: the formation of additional SrO structures interlayered with the perovskite phase under high pO_2 generates negatively charged Sr vacancies within the LSTO lattice, decreasing the population of free electrons, and lowering the conductivity; oxygen vacancies, generated under low pO_2 or reducing conditions, act as donor sites and increase the number of carriers available, increasing conductivity if the donated carriers are de-localized. This behavior under oxidizing and reducing conditions at high temperature initially made LSTO a subject of interest as a solid oxide fuel cell (SOFC) anode material[17, 21] and later as a sensing layer for optical and chemiresistive gas sensors[11, 12, 22, 23].

Metallic and other conducting nanoparticles are used in optical sensor applications due to the phenomenon of localized surface plasmon resonance (LSPR), the optical excitation of surface charge modes which is strongly dependent upon the near-field environment of the nanoparticle. The LSPR of metallic nanoparticles embedded within a medium can be modified both by passive interaction with the host material (e.g., change in the local index modifying the resonant condition) or more active interactions (e.g., charge transfer processes). In many cases, charge transfer is found to be most significant in explaining the gas sensing response at elevated temperatures[24]. Although variation of the index of refraction can also play a role, in the materials and conditions considered here, it is expected to provide a second-order contribution to the overall LSPR shift[25]. For optical sensing applications in high-temperature and chemically harsh environments, gold nanoparticles provide several benefits: a strong LSPR response (typically in the visible region of the spectrum), resistance to chemical activity, and stability at high temperature. In particular, gold nanoparticles are known to be stable in inert gas at the temperature ranges examined in this work, and although they have been demonstrated to show reactive evaporation in the presence of gases such as hydrogen and hydrogen sulfide at high temperature[26]; this behavior is known to be mitigated by encapsulating the nanoparticles within an oxide[27].

In this work, gold-nanoparticle incorporated LSTO sensing layers are investigated on a fiber optic sensing platform in chemically reducing gas streams at high temperature (600-800°C). The optical properties of this material system are examined on planar substrates under relevant, *in-situ* conditions, to help elucidate the physics governing the sensor response. The charge transfer mechanism between the conducting metal oxide film and nanoparticles is examined in detail as one possible mechanism governing the LSPR shift observed under reducing conditions. The interplay between the LSPR and the unique properties of the conducting matrix – high dopant concentration allowed by the perovskite structure and large static dielectric constant of LSTO – provides a complex optical response which can be processed to extract information about multiple process parameters, focusing here on hydrogen concentration and temperature. Principal component analysis (PCA) is utilized to determine what additional sensing information is provided by the LSPR response.

Methods and Materials

Sample Preparation

LSTO films on fiber and planar substrates were prepared respectively by dip-coating and spin-coating of a sol-gel solution, using a previously reported recipe [11, 25]. A molar ratio of lanthanum to strontium (7:3) was selected to ensure a high number of donor sites, while still maintaining La solubility under a broad range of oxidizing and reducing conditions. Directly prior to coating, gold chloride trihydrate ($HAuCl_4 \cdot 3H_2O$) was added to the solution at a concentration of 25 mg per 0.500 mL of solution (providing a molar ratio of approximately 0.07 gold atoms per Ti atom).

Planar samples were prepared on fused quartz substrates (Ted Pella, 1" diameter, 1/16" thick). Prior to coating, substrates were cleaned by sonicating in acetone (10 min.), ethanol (10 min.), and a 1 M solution of sodium hydroxide (45 min., with gentle heating; this step improves wetting of the sol gel solution on the substrate). Each sample was then rinsed in DI water and blown dry with nitrogen. Each sample was spin coated at 2.5 krpm for 60 s, after uniformly applying 200 μL of sol gel solution to the sample surface. Samples were then placed on a hot plate at 200°C for at least 15 minutes to remove any water from the coating, then calcined in a box furnace (Thermo Scientific Lindberg Blue M). The gold nanoparticles precipitate out into the film during the initial hot plate exposure, providing a broad distribution of nanoparticle sizes (as observed from SEM images, Fig. 3) with repeatable optical characteristics (i.e., LSPR peak and spectral width due to heterogeneous, size-based broadening). Calcination was performed in air – the temperature was ramped to 950°C (10 hrs.), held at 950°C (6 hrs.), then cooled to room temperature over at least 3 hrs.

To prepare the optical fiber samples, a 2" region of plastic jacket was stripped from the center of a 2-m length of Thorlabs LCA multi-mode fiber (Thorlabs FG105LCA, 105-μm diameter core, 125-μm external diameter with cladding, low-OH content). The stripped region was then immersed in a buffered HF solution (1:5 HF: NH_4F) for 1 hr., removing the cladding material and etching the fiber to a final diameter of approximately 95-μm (measured optically, a diagram and optical image of an etched fiber is shown in Figure 1). The fiber was rinsed in DI water, then soaked in 1 M NaOH for 1 hr. prior to coating. The fiber was hung vertically, and a droplet of precursor reserved in a pipette tip was run across the etched region from top to bottom. The coated region was briefly soft baked using a heat gun (~200°C) for 30 s, then transferred to a tube furnace for calcination. The calcination procedure was identical to that described for the planar samples.

Planar Sample Optical Measurements

For room-temperature, ambient air conditions, planar films were characterized using an Agilent Cary series UV-Vis-NIR spectrophotometer system. Both transmission and reflection spectra were measured at normal / near-normal incidence (reflectance measured at a 6° tilt relative to normal) in the spectral range of 200-2650 nm. Each spectrum was normalized relative to the transmission spectrum of the empty sample holder.

Optical transmission measurements at elevated temperature were performed in a high-temperature transmission cell with sapphire windows (Specac FT-NIR). Collimated light from a halogen lamp (Ocean Optics, DH-BAL) was used to illuminate the sample and the transmission spectrum was measured with a UV-Vis spectrometer (Ocean Optics Jaz, 190-890 nm). Each transmission spectrum was normalized relative to an empty cell (no sample present, but with two windows in place), under ambient conditions – i.e., room temperature, no gas flow.

Optical Fiber Based Measurements

The optical fiber sample was prepared as described above. The fiber was then placed in a custom-designed reactor system to allow both controlled gas flow composition and elevated temperature (Fig. 1). Light was coupled in from a halogen light source (Ocean Optics, DH-BAL). Two different detector configurations were used for transmission measurements. For collection of both the UV-Vis and NIR transmission spectra, the fiber was coupled to a commercial bifurcated fiber and split to a UV-Vis detector (Ocean Optics Jaz, 190-890 nm) and an NIR detector (ArcOptix FT-NIR Rocket 900 – 2600 nm). For measurements of the UV-Vis spectrum alone, the fiber was coupled directly to the Jaz spectrometer to provide higher signal. Transmission spectra shown in this work are normalized with respect to initial conditions, to emphasize changes in the transmission spectrum.

Gas Sensing Measurements

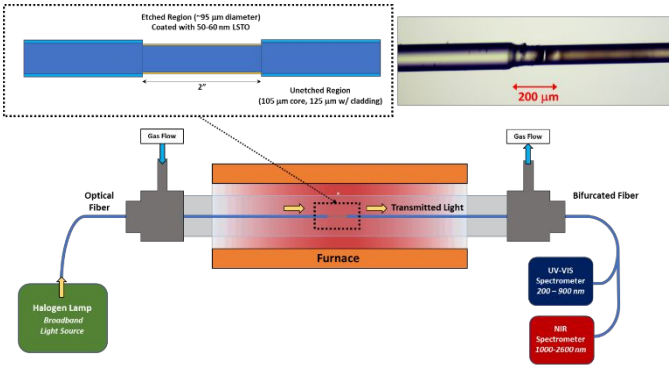

Figure 1. Diagram of the optical-fiber based measurements.

Both the optical transmission cell and reactor system (Fig. 1) described above are interfaced to an array of mass flow controllers, able to provide controllable gas flow conditions via a custom-built LabView interface. Three different gases are used in the experiments described here – UHP N_2, H_2, and O_2 – operating under a constant gas flow of 100 sccm at various compositions. Unless otherwise stated, a low-level flow of oxygen (1 sccm) is provided throughout each experiment to better control the pO_2 present in each step.

Film Microstructure and Crystallographic Characterization

To prevent applying conductive layers on top of the deposited films, scanning electron microscopy (SEM, Quanta 600F, FEI, USA) was conducted with a low-vacuum secondary electron detector (LFD) in the presence of water vapor.

Selected samples were prepared for cross-sectional transmission electron microscopy (TEM) analysis through standard focused ion beam (FIB) lift-out procedures which included mounting of the samples onto a copper grid and thinning to electron transparency by ion milling. An FEI NOVA dual-beam FIB was utilized with a Ga ion source in addition to the electron source as well as local Pt deposition for protection of the film during milling and welding to the copper grid. TEM analysis was performed using a Tecnai F20 Field Emission Gun (FEG) and a FEI Titan G2 80-300 TEM/STEM to obtain both conventional and high-resolution images for subsequent analysis and indexing.

Grazing-incidence x-ray diffraction (GI-XRD) scans were performed for films on planar quartz substrates using a PANalytical X'Pert Pro MRD with a Cu-Kα source (λ = 1.5405 Å) along 2θ from 20-69°. The ω(θ) angle was fixed at 1°. The scan data presented was collected by summing three scans, each performed at step sizes of 0.02°, integrating for 1 s / step.

Results

Planar Film Measurements

The optical response of the sensing layer on fiber is complicated by waveguiding effects and details of the optical fiber sensor preparation. Measurements of the planar film under similar

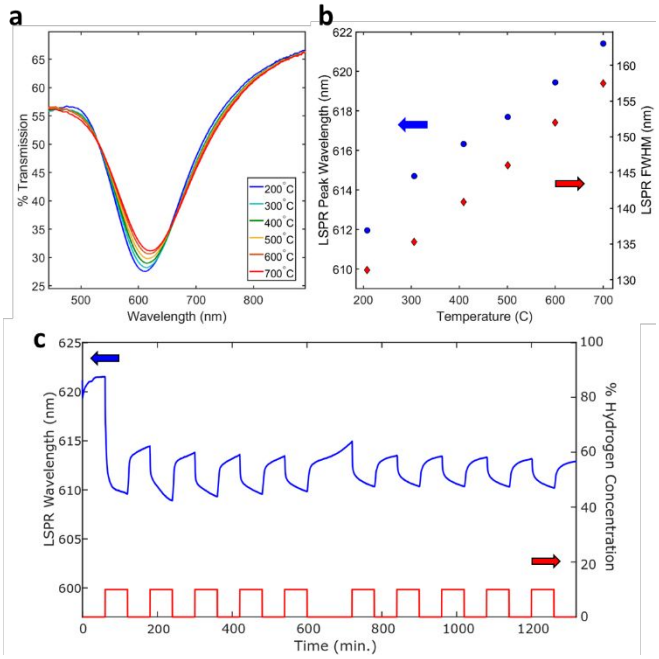

Figure 2. Optical transmission measurements of planar film at 700°C. (a) The transmission spectrum centered around the SPR, with varying temperature. (b) The change in the SPR band central wavelength and full-width-half-max (FWHM) as a function of temperature and (c) the central wavelength while cycling between 1% O2 and 10% H2 for a total of 22 hrs. (SPR wavelength shown in blue, % hydrogen concentration in red).

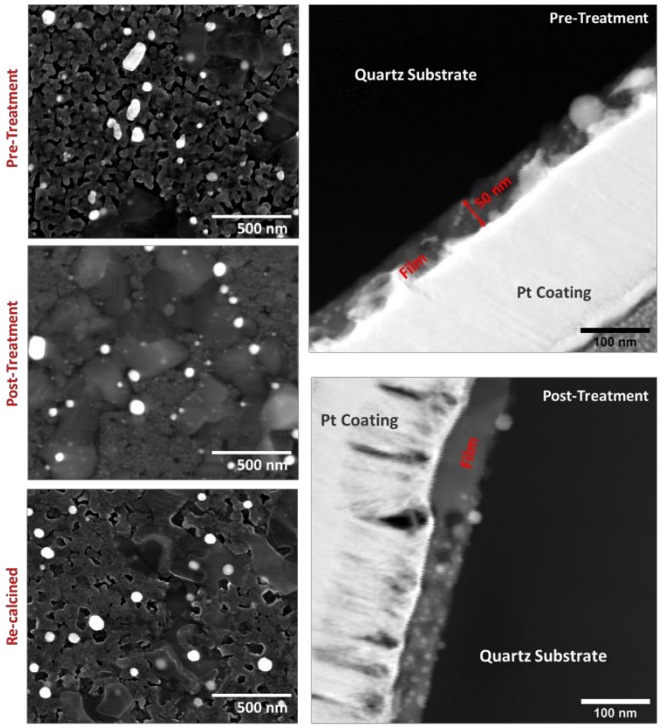

Figure 3. SEM (left) and dark-field TEM (right) images of gold nanoparticle incorporated LSTO film (top view and cross-section respectively). Pre-treatment images are of as-calcined film, post-treatment images are after 16 hrs. exposure to 10% H2 at 800°C. Re-calcined image is after repeating initial calcination in air.

conditions provides a simpler geometry to help clarify physical mechanisms at play and to allow direct monitoring of changes in sensing layer optical constants. The transmission profile of the thin film in the visible range is dominated by the LSPR absorption band, located near 600 nm at room temperature for the as-calcined film (Figure 2a). In the optical transmission cell, the transmission spectrum was measured as a function of temperature from 200°C to 700°C in air. Using a simple quadratic fit to the LSPR dip, the minima was tracked as a function of temperature; Fig. 2b demonstrates an approximately linear red shift of the LSPR peak wavelength from 610 nm to 622 nm over this temperature range. Broadening of the LSPR band is also estimated from the quadratic fit to the approximated absorptivity (log(1/T)) and is observed to increase from 131 nm at 200°C to 157 nm at 700°C, as a consequence of increased electron-phonon scattering with temperature[28]. After stabilizing in air for 1 hr. at 700°C, the sample was exposed to alternating, 1 hr. cycles of 1% O_2 and 10% H_2 (N_2 balance), with an additional 1 hr. of O_2 exposure after every 10 cycles. The hydrogen concentration profile is shown in Fig. 2c, along with the variation of the LSPR wavelength as a function of time. A fast, reversible blueshift of the LSPR is observed in response to hydrogen, starting off at 6 nm upon first exposure to hydrogen and stabilizing at approximately 3 nm (relative to 1% O_2).

To investigate the impact of long-term, high temperature exposure of the film to hydrogen, films with and without gold nanoparticles were exposed to 10% H_2 at 800°C for 16 hrs. (cooling to room temperature over 3 hrs. while maintaining a gas flow of 10% H_2). SEM images of the film before and after hydrogen exposure are shown in Figure 3, demonstrating coarsening of the oxide grains and coalescence of gold nanoparticles after high-temperature hydrogen exposure. Cross-sectional TEM images of the film before and after exposure confirm this trend, also illustrating the thickness of the film (~50 nm) and verifying that gold nanoparticles are distributed throughout the film, in addition to being present on the surface. A comparable SEM image of the hydrogen-treated film after re-calcination (repeating the calcination procedure in air) is also shown in Fig. 3, demonstrating that further modifications to the oxide are observed upon re-oxidation of the film under the original calcination conditions.

Further characterization of the crystallographic structure was performed on reduced and oxidized films (prepared identically to those described above) via glancing-incidence XRD, the results of which are shown in Figure 4a. Comparison with simulated spectra of gold and perovskite LSTO at the appropriate La concentration show that these phases are predominant in these films before and after hydrogen treatment, with no peaks observed from other phases. High-resolution TEM images (Figure 4b) of a typical gold nanoparticle embedded within the LSTO matrix additionally suggests a cube-on-cube orientation relationship between the two phases. In some regions, grains of the oxide matrix phase were difficult to index properly and exhibited superlattice structures (supplementary material, Fig. S1). Formation of superlattice structures within LSTO has been reported previously, as in the case of a Ruddelsden-Popper phase for example[20]. However,

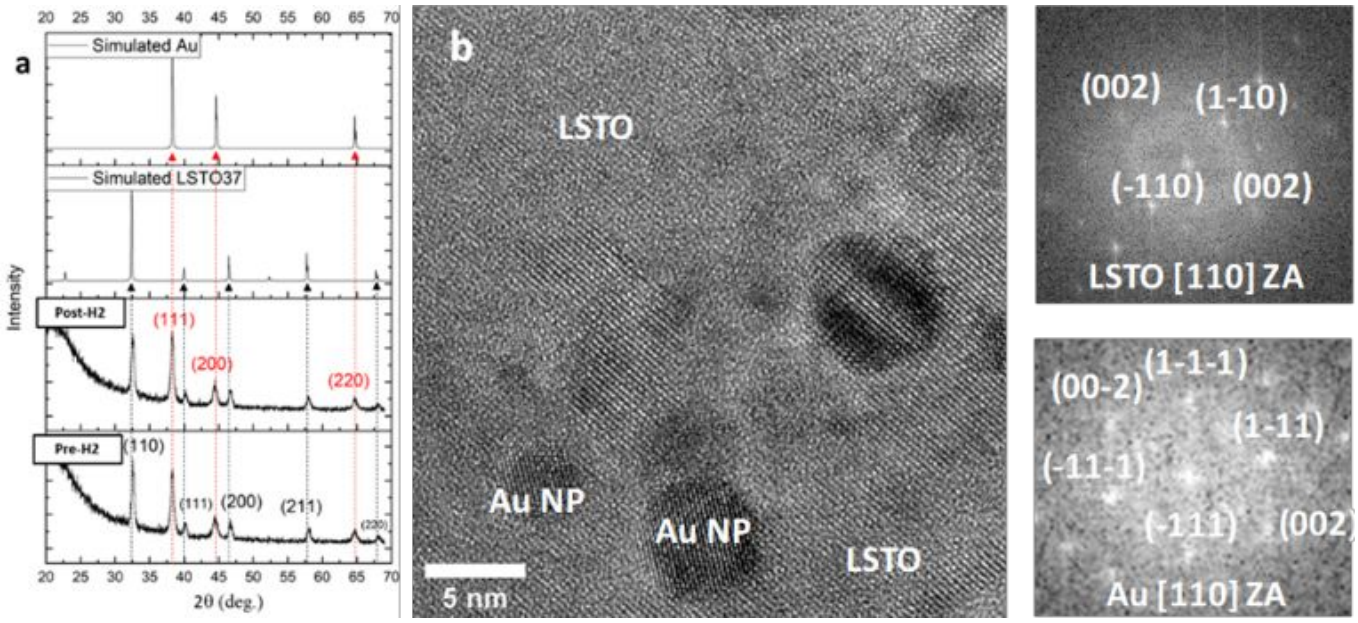

Figure 4. Crystallographic characterization of as-calcined and hydrogen treated films. (a) Glancing incidence XRD spectra of gold nanoparticle incorporated films on quartz substrate, before and after hydrogen treatment. Simulated peaks of LSTO (perovskite) and gold are shown. (b) High-resolution TEM image of gold nanoparticle (Au NP) within as-calcined film, showing approximate cube-on-cube relationship between gold and host film.

GI-XRD results can be fully indexed to the cubic perovskite phase and do not provide evidence for a significant volume fraction of additional phases.

The reflection and transmission spectra of gold-nanoparticle incorporated LSTO films were measured *ex-situ* in three different cases - (1) for the as-calcined film, (2) after hydrogen exposure, and (3) after re-calcination (i.e., subjecting the hydrogen-exposed film to the initial calcination at 950°C). In Figure 5a, the absorption coefficient is plotted as a function of wavelength for these three cases. The reflectance (R) and transmittance (T) were used to calculate the absorption coefficient (α):

$$\alpha = \frac{1}{d}\ln\left(\frac{1-R}{T}\right) \quad (1)$$

Based on TEM measurements (Fig. 3), a thickness (d) of 50 nm is used. Two features stand out in the absorption spectrum – the NIR absorption induced by the presence of free-carriers in the reduced samples and the shift of the LSPR absorption peak. Fig. 5b shows the same spectral data, expanding the wavelength window around the LSPR absorption peak of the gold nanoparticle incorporated films, illustrating a blue shift from 600 nm to 570 nm after hydrogen exposure. Both the LSPR shift and the free-carrier absorption are shown to disappear after re-calcination under oxidizing conditions.

Using a Cody-Lorentz oscillator model29 for the dielectric constant with a simple Drude term (to account for free-carrier absorption) and an Urbach term (to account for disorder related, sub-band absorption), fits were performed on the room temperature reflection and transmission curves of the films without gold nanoparticles (Supplementary Material, Figure S2; fitting parameters shown in Table S1). Based on these fits, estimates of the real and imaginary optical constants of the film were calculated for the as-calcined and hydrogen-treated films (Figs. 5c and 5d). The Drude term,

$$\varepsilon_{\text{Drude}} = -\frac{\omega_P^2}{\omega(\omega + i\tau^{-1})} \quad (2)$$

uses two free-parameters – the free-carrier plasma frequency (ω_P) and the damping rate (τ^{-1}). The fitted Drude parameters can be also used to estimate the carrier concentration (n),

$$n = \frac{\omega_P^2 \varepsilon_0 m^*}{e^2} \quad (3)$$

and mobility (μ)

$$\mu = \frac{e\tau}{m^*} \quad (4)$$

The effective mass in LSTO is believed to be approximately independent of the La dopant concentration up to the solubility limit - $m^* = 4.2m_0$[30]. The fitted free-carrier concentration of the reduced film associated with Fig. 5 corresponds to a carrier concentration of 1.6×10^{21} / cm^3 and mobility of 0.50 cm^2/V·s, which is consistent with previously reported results for LSTO (5.3×10^{21} / cm^3 for strongly reduced bulk samples with x = 0.30 La-fraction[19]).

Analysis of Charge Transfer

Metallic nanoparticles embedded in a semiconductor medium will naturally induce band banding of the semiconductor at the interface, as necessary to match the Fermi level at the boundary. This is achieved through charge transfer between the metallic nanoparticle and the semiconductor matrix, shifting the electrostatic potential of the particle and inducing a depletion region in the surrounding medium[26, 31]. The contact potential (V_0) and total charge transferred (n_q) can be calculated for a spherical nanoparticle by solving Poisson's equation, as demonstrated by Ionnides and Verykios[31],

$$V_0 = -\frac{eN_D}{\varepsilon_S}\left(\frac{W^2}{2} - \frac{r^2}{6} - \frac{W^3}{3r}\right) \quad (5)$$

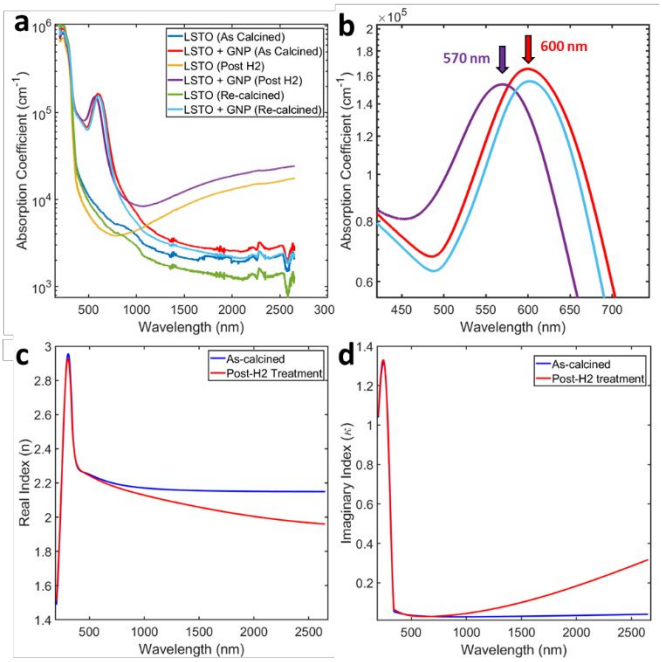

Figure 5. Optical absorption measurements of LSTO films (with and without gold nanoparticles) at room temperature. (a) Absorption coefficient of films as-calcined, after hydrogen treatment, and after re-calcination, (b) shows the same data as (a), near the LSPR absorption peak. (c) Real and (d) imaginary components of the refractive index are shown for films without gold-nanoparticles, before and after exposure, based on fits to the transmission and reflection curves (supplementary material, Fig. S3).

$$n_e = \frac{4\pi N_D}{3}(W^3 - r^3) \quad (6)$$

Notably, the LSPR response exhibits a longer timescale component not observed in the NIR (i.e., after 1 hr at fixed %H2, the NIR response at 700°C is relatively flat, while at 500-nm the response is still exhibiting a more "sawtooth" response).This behavior may be an important feature for distinguishing the mechanisms for plasmonic and free-carrier based response in LSTO. The Drude mechanism will ignore ionic contributions to the conductivity, due to the much larger ionic effective mass; however, the slow motion of ions / vacancies could impact

If the donor carrier density of the medium (N_D), nanoparticle radius (r), static dielectric constant (ε_S), and contact potential (V_0, equal to the work function difference (Φ_M-Φ_{SC})/e) are known, Eqn. 5 can be solved implicitly for the depletion width (W), which can then be used to calculate the total number of electrons transferred (n_e). In a medium with a high static dielectric constant, such as TiO_2 (50-100 for sputtered rutile film[32]) or $SrTiO_3$ (~300 at room temperature[33]) strong dielectric polarization necessitates a relatively large amount of charge transfer, with a correspondingly large depletion region, to balance out the potential difference (governed by the appearance of ε_S in the denominator of Eqn. 5). The expressions in Eqn. 5 and 6 rely on an approximation that the net charge in the depletion region is dominated by ionized donors which are distributed uniformly throughout the oxide matrix. Another consequence of the high dielectric constant of $SrTiO_3$ is that the donor states of La are extremely shallow and expected to be fully ionized at room temperature[34]. Applying material parameters for LSTO - $\varepsilon_S \approx 300$ and $m^* \approx 4.2\ m_0$ – to a hydrogenic model predicts a binding energy of 0.6 meV, far below the thermal energy at room temperature (k_BT = 26 meV).

Using Eqns. 5 and 6, the total charge transferred for a given film carrier density and nanoparticle radius can be calculated.

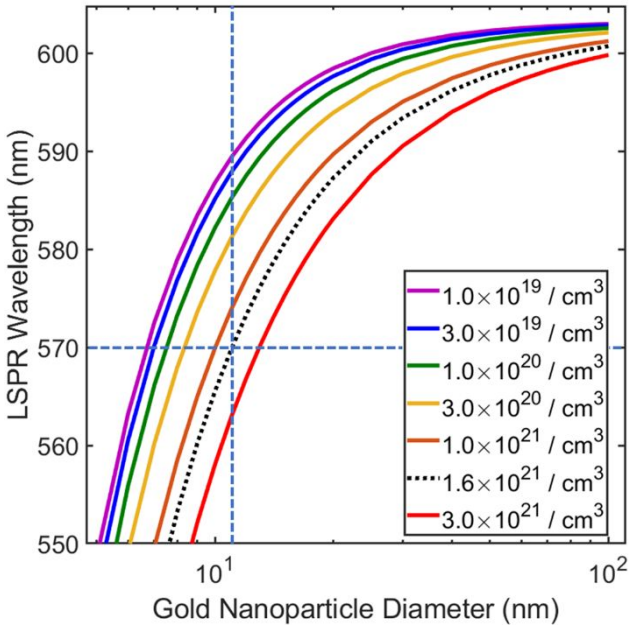

Figure 6. Calculated variation of the LSPR wavelength due to charge transfer as a function of gold nanoparticle diameter. Curves shown for different effective donor concentrations. Red curve and dotted black line indicate experimentally determined (fit) carrier concentration and LSPR, respectively. Blue dotted lines indicate cross-over point at 11-nm diameter.

Based on the optical fits associated with Fig. 5, the carrier density of the reduced films is 1.6×10^{21} / cm^3. Values for undoped $SrTiO_3$ are assumed for the work function difference at the gold interface (1.51 eV[35]) and static dielectric constant. Based on the total charge transferred and the nanoparticle size, the change in carrier concentration is calculated:

$$\frac{\Delta n_{GNP}}{n_{GNP}} = \frac{n_e \quad 1}{\frac{4}{3}\pi r^3 n_{GNP}} \quad (7)$$

The carrier concentration for bulk gold is $5.9\times10^{22}/cm^3$[36], but can also be inferred from the LSPR wavelength, as discussed below. For a nanoparticle that is much smaller than the wavelength of incident light (with complex dielectric constant $\varepsilon_{NP} = Re(\varepsilon_{NP}) + iIm(\varepsilon_{NP})$) embedded in an oxide (in this case LSTO, with complex dielectric constant ε_{LSTO}), the absorption cross-section is given by [37],

$$\sigma_{abs} \propto \frac{|\varepsilon_{LSTO}|^2 \quad Im(\varepsilon_{NP})}{Re(\sqrt{\varepsilon_{LSTO}})|\varepsilon_{NP} + 2\varepsilon_{LSTO}|^2} \quad (8)$$

The scattering cross-section will exhibit a resonance condition:

$$Re(\varepsilon_{NP}) + 2Re(\varepsilon_{LSTO}) = 0 \quad (9)$$

The imaginary components of the film dielectric constant lead to broadening of the absorption peak and can potentially lead to shifts as well if sufficiently large. From the optical fit in Fig. 5 the dielectric constant of the film near the LSPR can be estimated (n = 2.2, $Re(\varepsilon)$ = 4.8; the imaginary components - κ= 0.03, $Im(\varepsilon)$ = 0.13) do not impact the resonant wavelength significantly, but do introduce broadening of the resonance condition). The dielectric constant of gold near the LSPR is

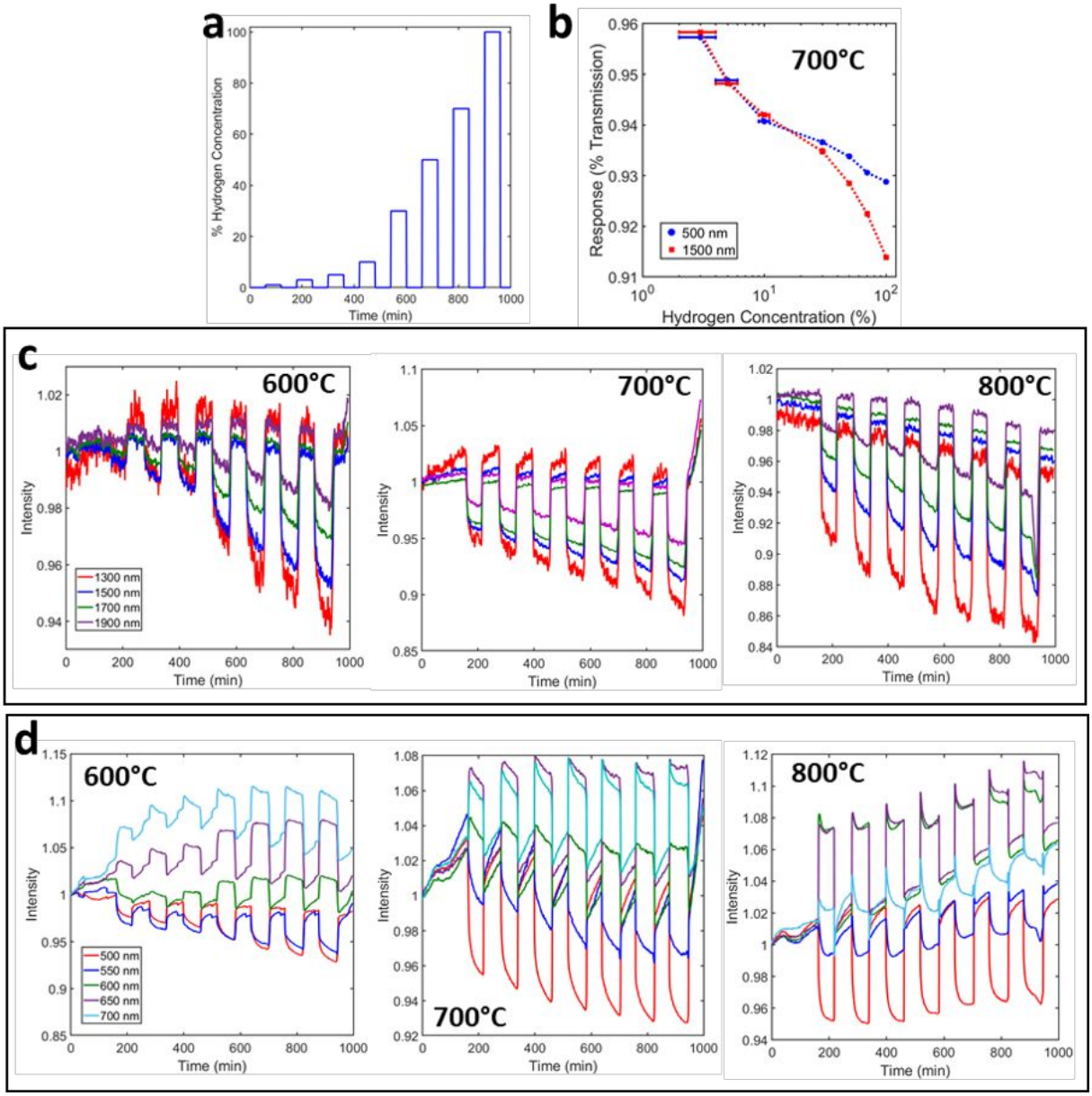

Figure 7. Optical transmission measurements of an etched fiber coated with gold-nanoparticle incorporated LSTO in hydrogen. (a) Hydrogen concentration levels as a function of time during each experiment at fixed temperature. (b) Equilibrium response (transmission during last 10 minutes of run) is shown at 500-nm and 1500-nm for fiber sensor at 700°C, with y-axis error bars indicating 95%-confidence intervals. Strip charts of the transmission at 600°C, 700°C, and 800°C are shown in (c) (NIR) and (d) (visible).

strongly dependent upon wavelength and is calculated using an analytical model from Etchegoin *et al*.[38]. This model includes the plasma frequency / wavelength as a parameter ($\omega_P = 2\pi\omega_P^{-1}$), which can be related to the gold nanoparticle carrier density through Eqn. 3. Using these parameters for the case of the oxidized film, with the LSPR resonance appearing at 602 nm (Fig. 5b), the carrier density of the relevant NPs contributing to the peak absorption is found to be $5.2\times10^{22}/cm^3$ (the effective electron mass is taken to be approximately equal to the free-space value, as is expected for bulk gold[39]). The full-width-half-max broadening of the LSPR, based on Eqn. 8 and not including heterogeneous broadening due to particle size inhomogeneity, is predicted to be 21 nm. Based on the amount of charge transfer predicted by Eqn. 7, this analytical model, in conjunction with the LSPR condition (Eqn. 9), is used to calculate the expected LSPR as a function of nanoparticle diameter for several different effective donor atom concentrations. This set of curves is plotted in Figure 6. Based on the observed LSPR and estimated free carrier concentration from Fig. 5, charge transfer involving nanoparticles approximately 11nm in diameter would explain the observed shift in the LSPR. For example, a carrier concentration of $1.6\times10^{21}/cm^3$ is estimated for the reduced films based on Fig. 5. For an 11-nm diameter nanoparticle Eqns. 5 and 6 can be solved numerically, resulting in a depletion width W = 10 nm and n_e = 4770 transferred per nanoparticle. The carrier concentration of gold is calculated based on the initial carrier density in the oxidized film ($5.2\times10^{22}/cm^3$) added to the additional transferred charge divided by the nanoparticle volume. Changing the plasma frequency, using the fitted permittivity for the reduced film, and recalculating the

permittivity of gold using the analytical model described above, results in an LSPR near 570 nm, as can be seen graphically in Fig. 6.

The carrier concentration of oxidized LSTO cannot be easily measured optically for a thin film, due to weak absorption in the NIR. It is assumed in this calculation that charge transfer is negligible for the oxidized film, although a small amount of LSPR shift is predicted by this model even at low carrier density levels, e.g., Fig. 6 shows an LSPR at 589 nm for $n = 1\times10^{19}/cm^3$. A more complete model would also need to consider changes in the local energetic landscape around GNPs during the annealing process, allowed by the mobility of oxygen and cation vacancies at high temperature, which may become frozen in during cooling and provide a significant contribution to the interface band offset between the nanoparticle and film, particularly in the oxidized case where free-carrier density is low.

Although the nanoparticles within the film are observed to have a broad size distribution (Fig. 3), this calculation indicates that charge transfer could, under reasonable assumptions, explain the experimental shifts observed. Note that the shift of the LSPR due to the change in the index of the host medium is small in this case, and insufficient to explain the magnitude of the observed shift[25]; using the same method of calculation (Eqn. 9), the permittivity of the host film would have to be approximately 3.90 (index of refraction, 1.97) to shift the LSPR peak to 570 nm. The change in index due to exposure to hydrogen, demonstrated in Fig. 5c, was insufficient to induce this change – using these fitted optical constants, an approximate red shift of 2 nm can be predicted for the reduced film, which does not match the observed effect in magnitude or sign.

Given that larger nanoparticles are expected to exhibit less shift within this model, an ideal sensing layer would be comprised only of smaller nanoparticles (~10 nm). Such a layer would necessarily have less heterogeneous broadening of the LSPR due to size variation and, as a result, would likely exhibit a sharper sensing response, both in terms of spectral width and response magnitude. The magnitude of response is expected to increase linearly with gold nanoparticle density (for a fixed size distribution), however non-linear variation may occur when the interparticle separation is less than the surface plasmon evanescent tail (on the order of λ) or when overlap of the depletion regions surrounding each nanoparticle occurs (~20-70 nm, based on the above calculations).

Hydrogen Response on Fiber

An etched optical fiber was prepared as described and the optical response to hydrogen was measured at 600°C, 700°C, and 800°C (Figure 7). At each temperature, the sample was cycled between 100 sccm N_2 and 100 sccm H_2 for ten hours prior to measurement. Then, the sample was exposed to varying levels of hydrogen concentration (Fig. 7a) in 1 hr. steps, with a 1 hr., 100 sccm N_2 recovery step between each hydrogen exposure (1 sccm O_2 maintained throughout). The equilibrium transmission response (λ = 500 nm and 1500 nm) as a function of hydrogen concentration at 700C is shown in Fig. 7b, Equilibrium values were defined as the mean during the last ten minutes of each cycle; error bars on the y-axis indicate the 95% confidence intervals. The transmission spectrum was obtained as a function of time in the visible and NIR in 15-s increments. Strip charts at several wavelengths of interest are shown for the NIR range (Fig. 7c) and visible range (Fig. 7d) at 600°C, 700°C, and 800°C.

At 700°C, the response and recovery times at 1500-nm were calculated as a function of hydrogen concentration. These quantities were defined as the time required to reach 90% of the response or recovery transmission value. These values (tabulated in the Supplementary Material, Table S2) ranged from 7.5-16 minutes for response and 3.6-14 minutes for recovery. Part of this response / recovery time can be attributed to the equilibration time of the gas flow system – with an approximate reactor volume of 500 mL, the expected fill time for the system is at least 5 minutes.

The NIR response of the sensing layer matches the free-carrier based absorption previously reported for LSTO films on fiber[11, 12, 22]. Throughout the NIR, absorption increases (transmission decreases) in response to the presence of hydrogen and then recovers in nitrogen (w/ 1% oxygen), with improved response at higher temperature.

The visible response is governed primarily by variation of the LSPR peak, as expected from the data acquired from planar films. In the presence of hydrogen, the LSPR absorption band blue shifts, lowering transmission in the range 450-600 nm and increasing transmission in the range 600-750 nm. Decreased transmission at the edge of the visible (>750 nm) in response to increasing H_2 concentration coincides with the response throughout the rest of the NIR. Like the free-carrier based response of the LSTO film, the LSPR response of the gold-nanoparticle incorporated film appears stronger at higher temperature. Both are expected to arise from the enhanced formation of oxygen vacancies which serve as donor impurities and sources of free electrons at high temperature under reducing conditions. For some other complex perovskite materials and oxides, incorporated hydrogen can itself contribute to the conductivity through carrier donation[40] or proton conduction[41]. Some experimental work indicates this impact is small relative to other mechanisms for single crystal $SrTiO_3$ [42], however the relative contribution carrier donation due to hydrogen incorporation provides relative to oxygen-vacancy based mechanisms is not determined. The baseline of the visible response, seen in Fig. 7d, is more stable at 700°C than 800°C. A significant component of the relatively slow overall drift to higher % transmission in the visible range can be explained by a gradual loss of gold that is expected to occur in the presence of hydrogen at elevated temperature, particularly above 700°C [26] (this is also observed in Fig. 5b, where the gold NP LSPR absorption peak drops irreversibly after annealing in hydrogen, remaining diminished even upon re-oxidation). This expected trend is evidenced by the results observed in Fig. 7d, where at 800°C the upward drift in transmission is most significant around 600-650 nm, consistent with a reduction of the LSPR absorption over time. It is likely that irreversible changes in the silica fiber also occur at this temperature (particularly under reducing conditions)[43, 44], but the

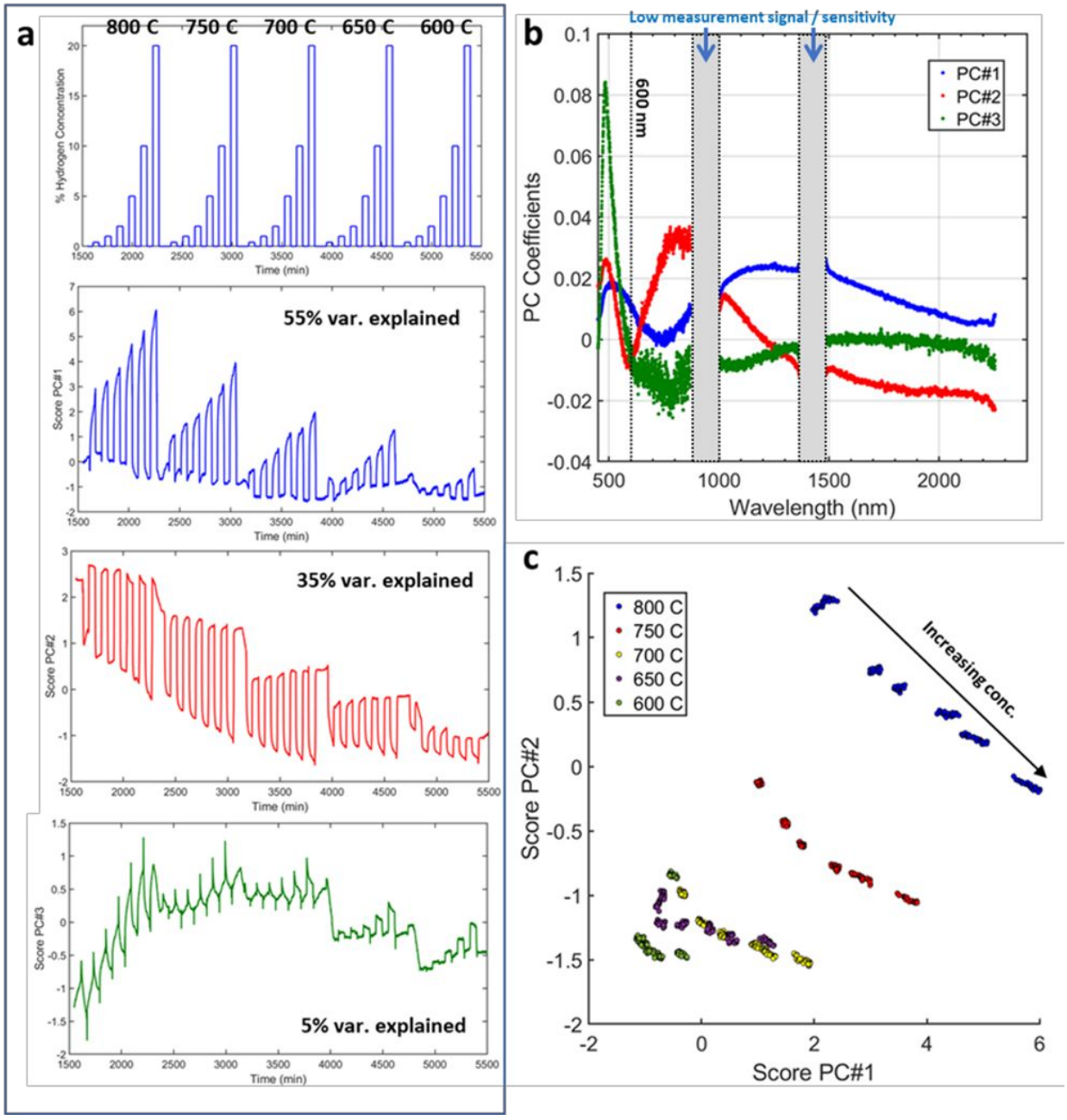

Figure 8. Summarized PCA of transmission spectra on fiber, simultaneously varying temperature and hydrogen concentration. (a) From top to bottom: the hydrogen concentration as a function of time, cycling from 0.4% to 20% at five temperatures (800°C, 750°C, 700°C, 650°C, 600°C) and the corresponding scores of the first three principal components. In (b), the coefficients of the first three PCs are shown in the original basis, mapped to wavelength. A map along the first two PCs is shown in (c), where each data point represents a single spectrum, excluding the recovery steps (in equilibrium only, 40-55 minutes into each step).

consequences of this evolution upon the transmission spectrum are more difficult to quantify.

Notably, the LSPR response also exhibits a longer timescale component not observed in the NIR (i.e., after 1 hr at fixed %H2, the NIR response at 700°C is relatively flat, while at 500-nm the response is still exhibiting a more "sawtooth" response).This behavior may be an important feature for distinguishing the mechanisms for plasmonic and free-carrier based response in LSTO. The Drude mechanism for the film itself will ignore ionic contributions to the conductivity, due to the large ionic effective mass; however, the slow motion of ions / vacancies could impact the local charge environment of the metal nanoparticles and impact the LSPR peak wavelength.

Gas / Temperature Cross-sensitivity and PCA

Like other metal oxides, one limitation of LSTO as a high temperature sensing material is that the sensing mechanism and associated NIR absorption are temperature-dependent and active to some extent for all chemically reducing gas streams. Previous work has shown that methane and carbon monoxide show a response that is qualitatively similar, but smaller in magnitude than that of hydrogen[12]. Prior work on ITO thin films has demonstrated that principal component analysis can be

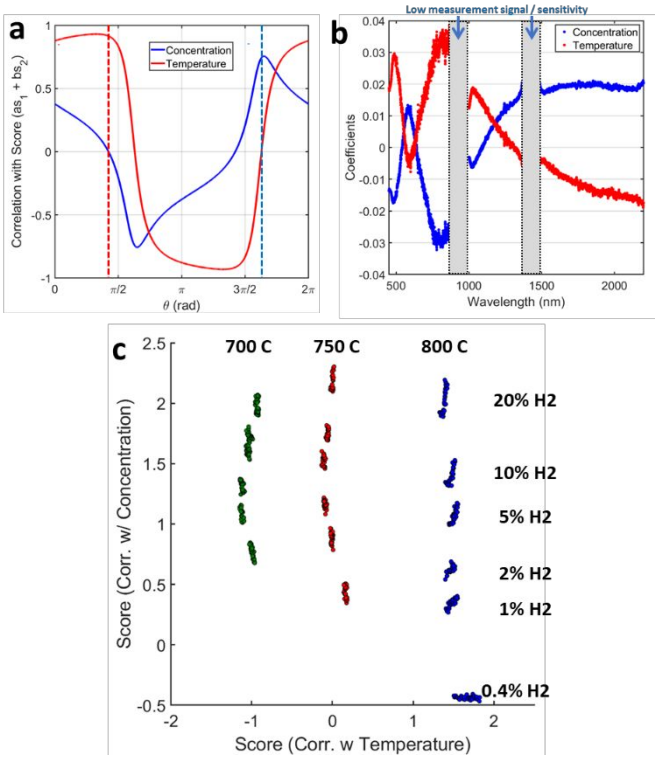

Figure 9. Transformation in plane of first two principal components to minimize correlation with process parameters. In (a), the correlation between score and the two process parameters – temperature and concentration – are plotted as a function of a new basis vector at some arbitrary angle in the plan between PC#1 and PC#2 from Fig. 8. Angles where score is individually / uniquely correlated to the two process parameters (i.e., correlated to concentration, uncorrelated to temperature, and vice versa) are shown with dotted lines. These angles define the new basis vectors in the PC#1-#2 plane, the coefficients which are shown in (b), using the original wavelength basis. The PC plot along these new axes is shown in (c).

used to correlate subtle changes in spectral characteristics for additional information (in particular, using variation in carrier concentration and mobility to improve gas cross-sensitivity discrimination)[9].

Principal component analysis (PCA) is a statistical method to determine the linearly independent components that most strongly contribute variance within a dataset. For multi-variate sensing applications, determining which principal components are more strongly correlated with different process variables is one approach to better discriminate subtle differences in response. Depending on the sensing mechanism for a material of interest, there is no guarantee that the process variables of interest will be necessarily uncorrelated with each other, meaning they will not necessarily be separately associated with distinct principal components. However, application of PCA coupled with an understanding of the underlying sensing mechanisms can be used to separate out subtle behavior in the sensor response (e.g., in Jee *et al.*[9], the distinct impact of the carrier concentration and mobility are separated out to improve gas cross-sensitivity discrimination of an optical-fiber based ITO sensing layer).

Transmission spectra were measured at a variety of temperatures and hydrogen concentrations, ranging from 0.4% to 20% (1% oxygen was only provided during the recovery step), as presented in Figure 8(a). Spectra were taken in UV-Vis and NIR regions, spectral regions with low signal were removed from the analysis: λ < 450 nm, 870 – 1010 nm (edge of spectrometer sensitivity), 1360-1480 nm (hydroxyl defect absorption in fiber), λ > 2250 nm (edge of spectrometer sensitivity and hydroxyl defect absorption in fiber). The remaining spectra were stitched together to form 3794 element arrays, each element mapped to a particular wavelength value. With an acquisition time set to 30 s, approximately 8000 spectra were collected over the entire run, resulting in a final data set in the form of a 3794 × 8000 matrix.

With the goal of uncovering the most physically meaningful principal components, the transmission spectrum was translated into an absorbance spectrum (ln(1/T)). The reason for dealing with this quantity is that multiple, uncorrelated absorption mechanisms (with absorption coefficients - α_1, α_2, etc.) within the film contribute multiplicatively to the decrease in transmission; e.g., for a thick film, thickness (d), ignoring reflections,

$$T(\lambda) = e^{-\alpha_1(\lambda)d} e^{-\alpha_2(\lambda)d} \quad (10)$$

Whereas,

$$\ln\left(\frac{1}{T(\lambda)}\right) = \alpha_1(\lambda)d + \alpha_2(\lambda)d \quad (11)$$

Given that PCA is a linear transformation / decomposition, the approach in Eqn. 11 is more likely to separate out independent absorption mechanisms. In practice it was observed that the difference between working with $T(\lambda)$ and -ln($T(\lambda)$) was small, primarily because the variation in this data set is relatively small relative to the average value (for small changes in the transmission, δT, relative to 100%, ln(1+δT) $\approx$ δT, so the response should be nearly linear with either approach).

PCA was performed on the entire time series of spectra. The first three principal components were found to explain a large majority of the variance (54.8% by PC#1, 35.0% by PC#2, 5.4% by PC#3, 0.7% by PC#4, 4.1% by all other PCs combined). The scores of the first three components are plotted as a function of time in Fig. 8a, the coefficients of these components are mapped to the wavelength values of the original spectra and plotted in Fig. 8b. As a point of reference, the approximate value of the room temperature, as-calcined LSPR is marked by a dotted line at 600 nm.

The values of these coefficients track the variance in the measured effective absorbance spectrum (as in Eqn. 11), the scores (Fig. 8a, lower three plots) indicate their relative contributions to the total measured spectrum at each point in time. The coefficients of the first principal component correspond to a blue shift of the LSPR (increased absorbance short-wavelength edge of the absorption band and decreased absorbance on the long wavelength edge), along with increasing absorbance in the NIR (the free carrier contribution). The second principal component primarily corresponds to a broadening of the LSPR (decreased absorbance near the LSPR peak, increased absorbance on both edges of the absorbance band) and decreased absorbance in the NIR. The score values of the first two PCs vs. time, shown in Fig. 8a, both exhibit a significant, reversible response to hydrogen. However, the score of PC#2 does not vary as significantly with concentration,

compared to PC#1. In Fig. 8c, each data point associated with hydrogen exposure in equilibrium (recovery steps are omitted, only spectra collected during the last 15 minutes of each step) is projected into the plane associated with the first two PCs. A clear trend is observed both in temperature and concentration, although spectra measured at lower temperature (< 700 C) appear to cluster together, indicative of a weakening response associated with these PCs. Note that at high temperature, the temperature response will appear in both broadening of the LSPR and changes in the NIR absorption (e.g., changing carrier mobility). In the lower temperature data, the LSPR broadening will still vary significantly with temperature, while the NIR absorption will diminish due to lower carrier concentration in this regime. This partially explains why the first two PCs show weakening response, while higher order PCs show better defined response within this range (such as PC#3, as observed in Fig. 8a).

The third principal component is dominated by absorption at short wavelength – this may be attributable to behavior of the sensing layer band edge (e.g., a Burstein-Moss shift due to changes in carrier concentration) or behavior of the silica fiber. Detailed investigation of the UV region of the spectrum would be necessary to explain this result more conclusively. At high temperature (700-800°C), the score of PC#3, shown in Fig. 8a, exhibits mainly transient response to changes in hydrogen, although a more stable response is observed at low temperature.

The purpose of PC analysis is to extract out the important features that contribute the most variance to the data set and classify individual data points relative to these features (using the score). However, the goal of analyzing sensor data is typically to map spectral data to the parameters of interest: temperature and gas concentration. There is no guarantee for a given sensor material that these goals will be aligned, particularly if the mechanisms which govern the sensor response are correlated to multiple parameters. And even then, there is no guarantee that the PC basis is the optimal one to the use for tracking these parameters. Instead, the "optimal" components from a sensor perspective would be individually responsive to one process variable of interest and completely unresponsive to all others.

In the analysis shown in Fig. 8, the scores associated with PCs #1 and #2 show distinct trends associated with concentration and temperature, on nearly perpendicular axes. To better separate out these trends, a new basis is chosen. To choose this new basis, a set of normalized coefficient vectors were defined at varying angle in the plane defined by the first two principal components (i.e., for PC's v_1 and v_2, $v = \cos(\theta)v_1+\sin(\theta)v_2$). The score associated the new vector was then calculated for each spectrum based on the scores of the first two PCs ($s_1(t)$,$s_2(t)$, both calculated at each point in the time series t) using the linear combination, $s_\theta(t) = \cos(\theta)\cdot s_1(t)+ \sin(\theta)\cdot s_2(t)$. In Figure 9(a), the linear correlation coefficient (ρ) of each new score was calculated with both temperature (T(t)) and gas concentration (c(t)) over $\theta = [0,2\pi]$, e.g., for concentration:

$$\rho_C(\theta) = \frac{\sum_{i=1}^{N}(c(t_i)-\bar{c})\cdot(s_\theta(t_i)-\overline{s_\theta})}{\sqrt{\sum_{i=1}^{N}(c(t_i)-\bar{c})^2\sum_{i=1}^{N}(s_\theta(t_i)-\overline{s_\theta})^2}} \quad (12)$$

The basis vectors within this plane were chosen to be the ones that minimized temperature correlation (5.12 rad., 293°) and minimized concentration correlation (1.33 rad., 76°) respectively over the equilibrium data. The coefficients of these new basis vectors are shown in Figure 9b (labeled by the process parameter they are correlated to). The coefficient that tracks most strongly with temperature, clearly corresponds to broadening of the LSPR, in conjunction with lowered free-carrier absorption, likely due to increased carrier scattering at higher temperature, which would lead to a reduction in the mobility. The coefficient that tracks most strongly with concentration includes increased absorption slightly offset to lower wavelength relative to the to the LSPR and increased NIR absorption. The influence of free-carrier concentration and mobility on the NIR region of the primarily principal components here is similar to was observed in prior PCA of ITO conducting thin films [9]. The scores of the high temperature data points from Fig. 8c are mapped onto this new basis in Fig. 9c, showing clear discrimination between the temperature and hydrogen response in the range 700-800°C.

This type of analysis can also be used to help guide light source / detector choices for more integrated sensor applications. For example, consideration of the coefficients presented in Figs. 9a and 9b suggests that for a single wavelength source, a wavelength near 1300 nm would be optimal for tracking concentration, because of the weak response to temperature at this wavelength. Alternatively, probing the response on the red- and blue-edges of the LSPR could be used (i.e., 800 nm and 500 nm) to simultaneously distinguish between concentration and temperature – as correlated changes between the two sensors would track temperature (broadening), anti-correlated changes would most closely track concentration (shift)[45-49].

Discussion

Through measurements of LSTO films incorporated with gold nanoparticles, it has been demonstrated that a significant LSPR shift is observed in the presence of a reducing gas flow at high temperature (600-800°C). This response co-exists and is interrelated with the established, free-carrier optical absorption present at NIR wavelengths for conducting metal oxides [11, 22]. Analysis of the charge transfer mechanism and its impact upon the LSPR wavelength indicate that this process is large enough in magnitude to explain the observed shift. The strong dielectric polarizability of $SrTiO_3$ – quantified by its high static dielectric constant (300) – necessitates an unusually large transfer of charge to embedded nanoparticles to equilibrate the work function difference between the film and metal, suggesting that doped strontium titanate is uniquely well-suited towards exploiting this sensing mechanism. High static dielectric constant is a feature strontium titanate shares with TiO_2, which similarly has been demonstrated as an excellent material for high temperature LSPR-based gas sensing[50, 51].

The response of gold-nanoparticle incorporated LSTO films to hydrogen has been demonstrated on an etched optical fiber platform, showing the strongest, most stable response at 700°C.

At lower temperature, the reduced LSPR response is correlated with the reduced free-carrier generation (a detailed summary of the physical mechanisms involved in free-carrier generation in reduced LSTO can be found in Schultz *et al*.[11]). At higher temperature, specifically above 800°C, some instability in the absorption response is introduced due to evaporative loss of gold from the film in the presence of hydrogen. Gold nanoparticles embedded within an oxide are known to be more stable in the presence of hydrogen, so it is likely that this drift is preferentially caused by gold sitting on the surface. In both cases, gold loss can be mitigated by the introduction of an additional, thin oxide layer on top of the sensing layer[12]. Reactive evaporation aside, it is also known that silica fiber is unstable in the presence of hydrogen at high temperature, so further development on this platform for highly reducing conditions will also be contingent upon the development of enhanced stability fibers at scale, with single-crystal fibers of high temperature materials such as sapphire being the current primary approach being explored in the literature[8].

Conclusions

The LSPR-based response of gold-nanoparticle incorporated LSTO to hydrogen at elevated temperatures (600-800°C), reported here on an optical fiber based sensing platform, serves to complement the NIR based response of conducting metal oxide films, lending both flexibility in terms of detector choice and additional information that can be used for discrimination between different types of reducing gases. Charge transfer between the conducting perovskite film and the nanoparticles is suspected to be the dominant mechanism for LSPR shift in response to exposure to hydrogen. Although these two mechanisms – free-carrier absorption and charge-transfer governed LSPR shift - are physically correlated, differences of the physical mechanisms and their relative response to different gases provides distinct absorption behaviour that can be resolved using techniques such as principal component analysis. Furthermore, the material properties of LSTO – stability at high temperature and under a wide variety of chemically reactive conditions, good electrical conductivity / NIR optical absorption under these conditions, and dielectric properties conducive to significant oxide-metallic nanoparticle charge transfer – make it well suited to this application.

Conflicts of interest

There are no conflicts to declare.

Acknowledgements

This work was performed in support of the US Department of Energy's Fossil Energy Crosscutting Technology Research Program and was executed through the NETL Research and Innovation Center's Advanced Sensors and Controls Field Work Proposal. Research performed by Leidos Research Support Team staff was conducted under the RSS contract 89243318CFE000003.

This research was supported in part by an appointment to the National Energy Technology Laboratory Research Participation Program, sponsored by the U.S. Department of Energy and administered by the Oak Ridge Institute for Science and Education.

The authors would like to acknowledge use of the Materials Characterization Facility at Carnegie Mellon University under grant # MCF-677785.

The authors wish to thank Dr. Bret Howard for providing x-ray diffraction measurements of sol-gel derived powders to assist in the material development. They also wish to thank Drs. Subhabrata Bera and Ki-Joong Kim for many valuable discussions pertaining to the sol gel solution chemistry.

Disclaimer

This work was funded by the Department of Energy, National Energy Technology Laboratory, an agency of the United States Government, through a support contract with Leidos Research Support Team (LRST). Neither the United States Government nor any agency thereof, nor any of their employees, nor LRST, nor any of their employees, makes any warranty, expressed or implied, or assumes any legal liability or responsibility for the accuracy, completeness, or usefulness of any information, apparatus, product, or process disclosed, or represents that its use would not infringe privately owned rights. Reference herein to any specific commercial product, process, or service by trade name, trademark, manufacturer, or otherwise, does not necessarily constitute or imply its endorsement, recommendation, or favoring by the United States Government or any agency thereof. The views and opinions of authors expressed herein do not necessarily state or reflect those of the United States Government or any agency thereof.

Footnotes and references

1. P. Ohodnicki, S. Credle, M. Buric, R. Lewis and S. Seachman, 2015.
2. B. Chorpening, D. Tucker and S. Maley, 2004.
3. R. R. Romanosky and S. M. Maley, 2013.
4. E. G. T. Services, *Fuel cell handbook [electronic resource] / EG&G Technical Services, Inc*, U.S. Dept. of Energy, Office of Fossil Energy, National Energy Technology Laboratory, Morgantown, WV, 2004.
5. G. W. Hunter, P. G. Neudeck, C. Liu, B. Ward, Q. Wu, P. Dutta, M. Frank, J. Trimbol, M. Fulkerson and B. Patton, 2002.
6. E. Udd, W. L. Shulz, J. M. Seim, M. Morrell, T. L. Weaver, J. Bush and G. Adamovsky, 1999.
7. D. G. Senesky, B. Jamshidi, K. B. Cheng and A. P. Pisano, *IEEE Sensors Journal*, 2009, **9**, 1472-1478.
8. H. Chen, M. Buric, P. R. Ohodnicki, J. Nakano, B. Liu and B. T. Chorpening, *Applied Physics Reviews*, 2018, **5**, 011102.
9. Y. Jee, Y. Yu, H. W. Abernathy, S. Lee, T. L. Kalapos, G. A.

Hackett and P. R. Ohodnicki, *ACS applied materials & interfaces*, 2018, **10**, 42552-42563.
10. Z. L. Poole, P. Ohodnicki, R. Chen, Y. Lin and K. P. Chen, *Optics Express*, 2014, **22**, 2665-2674.
11. A. M. Schultz, T. D. Brown and P. R. Ohodnicki Jr, *The Journal of Physical Chemistry C*, 2015, **119**, 6211-6220.
12. M. Yan, J. Tylczak, Y. Yu, G. Panagakos and P. Ohodnicki, *Sensors and Actuators B: Chemical*, 2018, **255**, 357-365.
13. P. Ohodnicki Jr, M. Andio and C. Wang, *Journal of Applied Physics*, 2014, **116**, 024309.
14. P. R. Ohodnicki Jr, C. Wang and M. Andio, *Thin Solid Films*, 2013, **539**, 327-336.
15. L. G. Tejuca and J. L. Fierro, *Properties and applications of perovskite-type oxides*, CRC Press, 1992.
16. T. Ishihara, *Perovskite oxide for solid oxide fuel cells*, Springer Science & Business Media, 2009.
17. O. A. Marina, N. L. Canfield and J. W. Stevenson, *Solid State Ionics*, 2002, **149**, 21-28.
18. R. Moos, T. Bischoff, W. Menesklou and K. Hardtl, *Journal of Materials Science*, 1997, **32**, 4247-4252.
19. R. Moos, S. Schöllhammer and K. Härdtl, *Applied Physics A*, 1997, **65**, 291-294.
20. U. Balachandran and N. Eror, *Journal of the Electrochemical Society*, 1982, **129**, 1021-1026.
21. S. Suthirakun, G. Xiao, S. C. Ammal, F. Chen, H.-C. zur Loye and A. Heyden, *Journal of Power Sources*, 2014, **245**, 875-885.
22. A. M. Schultz, T. D. Brown, M. P. Buric, S. Lee, K. Gerdes and P. R. Ohodnicki, *Sensors and Actuators B: Chemical*, 2015, **221**, 1307-1313.
23. W. Menesklou, H.-J. Schreiner, K. H. Härdtl and E. Ivers-Tiffee, *Sensors and Actuators B: Chemical*, 1999, **59**, 184-189.
24. J. P. Baltrus, P. R. Ohodnicki, N. A. Joy and M. A. Carpenter, *Applied Surface Science*, 2014, **313**, 19-25.
25. J. Wuenschell, Y. Jee and P. Ohodnicki, 2019.
26. J. P. Baltrus, G. R. Holcomb, J. H. Tylczak and P. R. Ohodnicki, *Journal of The Electrochemical Society*, 2017, **164**, B159-B167.
27. N. A. Joy, B. K. Janiszewski, S. Novak, T. W. Johnson, S.-H. Oh, A. Raghunathan, J. Hartley and M. A. Carpenter, *The Journal of Physical Chemistry C*, 2013, **117**, 11718-11724.
28. O. Yeshchenko, I. Bondarchuk, V. Gurin, I. Dmitruk and A. Kotko, *Surface Science*, 2013, **608**, 275-281.
29. A. Ferlauto, G. Ferreira, J. M. Pearce, C. Wronski, R. Collins, X. Deng and G. Ganguly, *Journal of Applied Physics*, 2002, **92**, 2424-2436.
30. R. Moos, A. Gnudi and K. H. Härdtl, *Journal of applied physics*, 1995, **78**, 5042-5047.
31. T. Ioannides and X. E. Verykios, *Journal of Catalysis*, 1996, **161**, 560-569.
32. M. Takeuchi, T. Itoh and H. Nagasaka, *Thin Solid Films*, 1978, **51**, 83-88.
33. B. Choudhury, K. Rao and R. Choudhury, *Journal of Materials Science*, 1989, **24**, 3469-3474.
34. A. Verma, A. P. Kajdos, T. A. Cain, S. Stemmer and D. Jena, *Physical Review Letters*, 2014, **112**, 216601.
35. J. E. Carnes and A. M. Goodman, *Journal of Applied Physics*, 1967, **38**, 3091-3096.
36. P. Fulay and J.-K. Lee, *Electronic, magnetic, and optical materials*, Crc Press, 2016.
37. S. Nordebo, M. Dalarsson, Y. Ivanenko, D. Sjöberg and R. Bayford, *Journal of Physics D: Applied Physics*, 2017, **50**, 155401.
38. P. G. Etchegoin, E. Le Ru and M. Meyer, *The Journal of chemical physics*, 2006, **125**, 164705.
39. J. Szczyrbowski, *Journal of Physics D: Applied Physics*, 1986, **19**, 1257.
40. C. G. Van de Walle, *Physical review letters*, 2000, **85**, 1012.
41. K.-D. Kreuer, *Annual Review of Materials Research*, 2003, **33**, 333-359.
42. M. Widerøe, R. Waser and T. Norby, *Solid state ionics*, 2006, **177**, 1469-1476.
43. L. Yu, E. Bonnell, D. Homa, G. Pickrell, A. Wang, P. Ohodnicki Jr, S. Woodruff, B. Chorpening and M. Buric, *Optical Fiber Technology*, 2016, **30**, 1-7.
44. L. Yu, D. Homa, P. Ohodnicki Jr, M. Buric, B. Chorpening, G. Pickrell and A. Wang, *Optical Fiber Technology*, 2019, **52**, 101951.
45. P. R. Ohodnicki, M. P. Buric, T. D. Brown, C. Matranga, C. Wang, J. Baltrus and M. Andio, *Nanoscale*, 2013, **5**, 9030-9039.
46. P. R. Ohodnicki Jr, T. D. Brown, G. R. Holcomb, J. Tylczak, A. M. Schultz and J. P. Baltrus, *Sensors and Actuators B: Chemical*, 2014, **202**, 489-499.
47. N. M. Houlihan, N. Karker, R. A. Potyrailo and M. A. Carpenter, *ACS sensors*, 2018, **3**, 2684-2692.
48. N. A. Joy, M. I. Nandasiri, P. H. Rogers, W. Jiang, T. Varga, S. V. Kuchibhatla, S. Thevuthasan and M. A. Carpenter, *Analytical chemistry*, 2012, **84**, 5025-5034.
49. N. A. Joy, P. H. Rogers, M. I. Nandasiri, S. Thevuthasan and M. A. Carpenter, *Analytical chemistry*, 2012, **84**, 10437-10444.
50. P. R. Ohodnicki Jr, C. Wang, S. Natesakhawat, J. P. Baltrus and T. D. Brown, *Journal of Applied Physics*, 2012, **111**, 064320.
51. P. R. Ohodnicki, T. D. Brown, M. P. Buric, J. P. Baltrus and B. Chorpening, 2012.

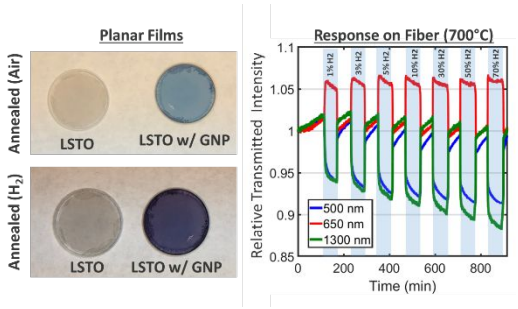

Coupled plasmonic and Drude response of gold-nanoparticle incorporated LSTO demonstrates visible and NIR fiber-based sensing of hydrogen at high-temperature (600-800°C).